Role of vertical ion convection in the high-latitude ionospheric plasma distribution

Y. Deng[1] and A. J. Ridley[1]

[1] We use the Global Ionosphere-Thermosphere Model (GITM) to simulate the ionospheric reaction to a simple step change of the high-latitude forcing terms during the first hour of electric field enhancement. In response to the enhanced convection electric field, both the convection velocity and Joule heating increase dramatically. The changes in NmF_2 present that the tongue extends across the polar cap and the troughs stretch longitudinally. The calculated total electron content (TEC) can vary by 15 TECU and have a similar pattern to the changes of NmF_2. The changes in the vertical ion drift can be upward 100 m/s on the dayside and downward 100 m/s on the nightside as a consequence of the changes in the $\mathbf{E} \times \mathbf{B}$ drift. Approximately, hmF_2 ascends where V_{iR} is upward and descends where V_{iR} is downward. In general, the response of the ionosphere to the enhanced E-field is that the F_2 layer moves upward on the dayside and enhances at all altitudes on the nightside. Below the F_2 peak (250 km altitude), the region of decreasing electron density coincides with the upward V_{iR} on the dayside, and the reverse is true on the nightside. Above the F_2 peak (450 km altitude), the features related with both horizontal convection and vertical advection are present. The vertical ion drift sets up a vertical circulation in the noon-midnight meridional plane during the early stage of E-field enhancement in addition to the widely accepted horizontal two cell convection. According to the circulation, the significant sources of tongue ionization are not only the plasma from the lower latitudes, but also from the low altitudes on the dayside. While the vertical circulation is not well organized after 6-hour E-field enhancement, the contribution of vertical ion convection is still significant. Although the vertical $\mathbf{E} \times \mathbf{B}$ drift in Apex coordinates is more complex and variable than that in a simple dipole magnetic field, the main characteristics are the same, which indicate the significance of the vertical circulation for the electron density distribution in reality during the early stage of E-field enhancement. The Joule heating drives upwelling of the atmosphere and modifies the O/N_2 ratio. Meanwhile, the enhanced neutral advection twists the O/N_2 ratio pattern a little bit. However, the changes in the O/N_2 ratio have relatively poor correlation with the variation of electron density during the first hour of E-field enhanced time.

1. Introduction

[2] During storm times, complex disturbances in the ionosphere and thermosphere can cause both increases and decreases in the F_2 peak electron density, or ionospheric positive and negative storm phases, respectively [*Prölss*, 1997; *Fuller-Rowell et al.*, 1997; *Buonsanto*, 1999; *Schunk and Nagy*, 2000; *Lu et al.*, 2001]. The electron density profile is very important, possibly changing the total electron content (TEC) and hence affecting GPS measurements [*Hajj et al.*, 1994; *Mitchell and Spencer*, 2003; *Yin et al.*, 2004]. It is widely accepted that the increase of Joule heating in high latitudes is the primary driver to the global thermosphere-ionosphere perturbation [*Banks*, 1977]. Since Joule heating is proportional to the plasma density, a precise knowledge of the ionosphere in the polar region is important for Joule heating and the consequent storm phases.

[3] Many studies have examined the high-latitude electron density behavior during storms. For example, the expanded and enhanced convection electric field [*Foster et al.*, 1986; *Knipp et al.*, 1989] extends the tongue of ionization over the polar cap (positive phase) and moves the trough features to lower latitudes (negative phase) [*Sojka and Schunk*, 1983; *Prölss et al.*, 1991; *Schunk and Sojka*, 1996; *Crowley et al.*, 1996; *Schunk and Nagy*, 2000]. The increased electric field, combined with the increased plasma density, increases the Joule heating, raising the upper thermospheric temperatures, thereby lifting the thermo-

---

[1]Center for Space Environment Modeling, University of Michigan, Ann Arbor, Michigan, USA.
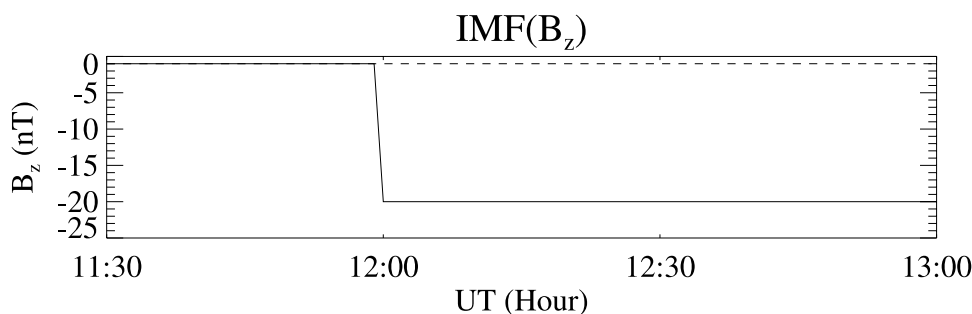
IMF(B_z)

Figure 1. Time variation of the IMF B_z during the simulations. Solid line is the E-field enhanced case; dotted line is the background case.

sphere up [*Maeda et al.*, 1989; *Prölss*, 1980, 1997] and causing density and composition perturbations at higher altitudes.

[4] These perturbations are not limited to the polar region. They are transported from high to mid-low latitudes through traveling atmospheric disturbances (TADs) and large-scale storm circulation [*Fuller-Rowell et al.*, 1994; *Prölss et al.*, 1991; *Prölss*, 1993; *Bauske and Prölss*, 1997; *Tsagouri et al.*, 2000], which drive the F region to higher altitudes and cause positive ionospheric storm phases at midlatitudes. Meanwhile, the changes of neutral composition (decrease of O/N_2) are also transported to midlatitudes and lead to electron density decreases [*Rishbeth et al.*, 1987; *Prölss*, 1987; *Field et al.*, 1998; *Burns et al.*, 1991; *Fuller-Rowell et al.*, 1997], termed a negative storm phase. In addition, electric field penetration into midlatitudes [*Foster et al.*, 1998; *Sojka et al.*, 2002; *Huang et al.*, 2005], which is related to dynamics in both high-latitude electric field and storm time ring currents, can contribute to both positive and negative storm phases. *Pavlov and Foster* [2001] and *Richards and Torr* [1986] documented that the vibrationally excited N_2 and O_2 can reduce the F-region peak density substantially.

[5] While it is understood that the coexistence of many effects causes various changes in the ionosphere, these effects have not been thoroughly quantified. *Sojka et al.* [1981] qualitatively analyzed the effect of vertical electrodynamic drift on the ion density profiles at high latitudes. Besides these studies, little attention has been paid to the effects of the vertical component of the $\mathbf{E} \times \mathbf{B}$ drift in the polar region, while the influence of horizontal ion convection and neutral composition have been well studied. Here Global Ionosphere Thermosphere Model (GITM) is used to investigate the polar region ionosphere reaction to a simple step change of the high-latitude forcing terms. Because GITM relaxes the hydrostatic equilibrium condition on the thermosphere, significant vertical winds are able to form because of nongravitational forces such as ion drag, coriolis, and centrifugal acceleration. The changes of vertical ion drift and its impact on the F_2 layer are presented during the first hour of electric field enhancement in equinox seasons. Then, the relative importance of different mechanisms is examined, including horizontal advection, vertical advection and chemical reactions on both the bottomside (Alt = 250 km) and topside (Alt = 450 km) of the F_2 layer. The

correlation between the O/N_2 ratio and electron density in a nonequilibrium situation is also investigated.

2. Inputs for the Global Model

[6] GITM is a new model of the coupled ionosphere and thermosphere [*Ridley et al.*, 2006]. It is different than other global ionosphere thermosphere models in that it relaxes the hydrostatic equilibrium condition on the thermosphere, allowing significant vertical winds to form because of nongravitational forces such as ion drag, coriolis, and centrifugal acceleration. The simulations described in this study are all started from MSIS and IRI, with static neutrals. Without special declaration, the magnetic field is from a simple dipole field model. We use the *Weimer* [1996] electrodynamic potential patterns and the *Fuller-Rowell and Evans* [1987] particle precipitation patterns as high-latitude drivers. The model resolution is 2.5° latitude by 5° longitude by approximately 1/3 scale height initially.

[7] The initial conditions are equinox, moderate solar activity ($F_{10.7} = 150$), and quiet geomagnetic activity (Hemisphere Power = 10GW, Interplanetary Magnetic Field $B_z = -1$ nT). GITM is run with these initial conditions for 12 hours to reach a quasi-steady state. We then change B_z from −1 to −20 nT, as shown in Figure 1, while all other inputs are held constant. It is defined as an electric field enhanced case. The particle precipitation is constant in our simulation, because we want to separate the effect of an increased convection electric field from that of particle precipitation and emphasize the contribution from the convection electric field. In a typical storm, such a change in the IMF Bz (from −1 to −20 nT) can cause significant enhancements of particle precipitation, which increase the ionization in the auroral zone due to the precipitated particle impact on the neutral atmosphere. Therefore there will be also some increase of electron density in the auroral region as a consequence of the particle precipitation enhancement, which is not included in this study.

[8] In a real event, there is a time delay between the IMF measurement of an upstream satellite (ACE, WIND, IMP-8, Geotail, or Interball) and change of ionospheric electric field. For example, *Ridley* [2000] examined the error in techniques for computing time delays, and *Ridley et al.* [1997] examined the time delay between when the change in IMF reached the magnetopause and when the ionospheric convection started to change. However, this time delay is
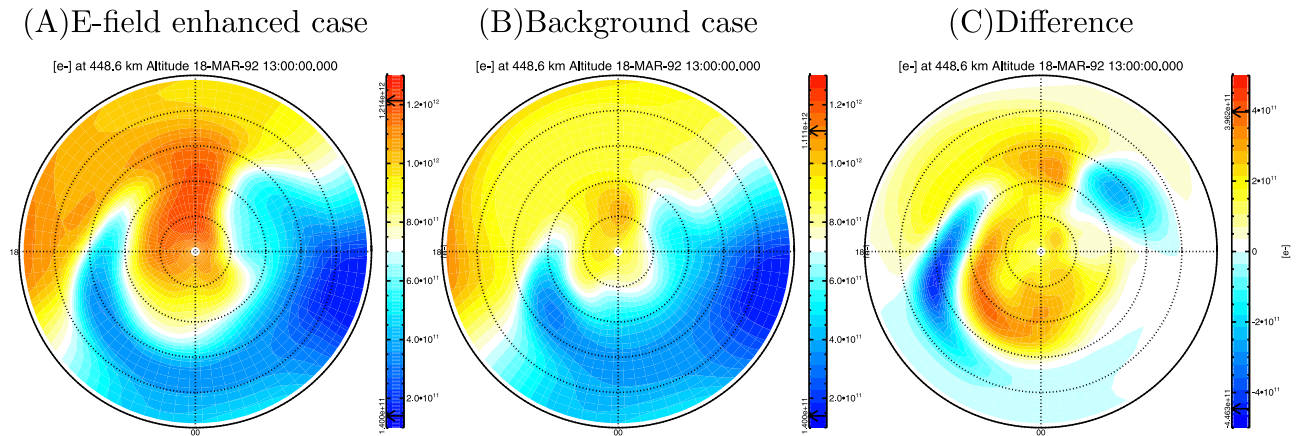
(A)E-field enhanced case   (B)Background case   (C)Difference

Figure 2. Electron density distribution in the (a) E-field enhanced case and (b) background case at 1300 UT. (c) Difference between the E-field enhanced case and the background case. All of them are in the northern polar region and equinox seasons. The outside ring is 40°.

not relevant to this study. What we are specifically examining is the response of the ionospheric electron density caused by the electric field changes. IMF B_z is used to specify the electric field change, because that is the primary driver for almost all modern empirical models of the ionospheric potential. To compare this to a real storm, one would have to examine AMIE or SuperDARN electric potential maps, and would compare GITM results to the real ionosphere at the time when those potential maps showed significant increases in the potential.

[9] The time interval being investigated is the first hour after the electric field is enhanced, which is much shorter than a storm period (~12 hours or one day, as in the works by *Fuller-Rowell et al.* [1994], *Tsagouri et al.* [2000] and *Lu et al.* [2001]). While some studies have been done concerning the effects of the effects of the low-latitude penetrating electric field, relatively few papers actually examine the "first response" at high latitudes to an electric field enhancement. In addition, after the electric field increases abruptly, the ion velocity rises instantly. However, it will take several hours for the neutral wind to totally ramp up. During the first hour, when the ion velocity already increases dramatically but the neutral wind, the velocity of neutral constituent, just begins to change, the difference between ion velocity and neutral wind, and hence Joule heating, can be large compared with the values in the

subsequent times. Therefore the changes of ion density in the first hour have significant consequences on the whole ionosphere-thermosphere system.

[10] During times of enhanced electric field, a tongue of ionization extends over the polar cap and the trough features move to lower latitudes, as shown in Figure 2a. Figure 3 shows both the tongue and trough features clearly along the DMSP satellite trajectory, which are consistent with observations [*Foster et al.*, 2005]. In an attempt to isolate the response of the ionosphere to the electric field change, we calculate the differences (Figure 2c) between the enhanced electric field case (Figure 2a) and the background case (Figure 2b), which is run with the initial conditions described in section 3.2. All of the subsequent contour figures display differences in the parameters with respect to the background values.

3. Results

[11] Figure 4 summarizes the main perturbations and couplings in the thermosphere-ionosphere during the enhanced electric field period. After the electric field is enhanced, the electron density is affected by three processes: (1) horizontal plasma convection, which redistributes the electron density in the polar region; (2) vertical ion transport, which is driven by both the vertical component of
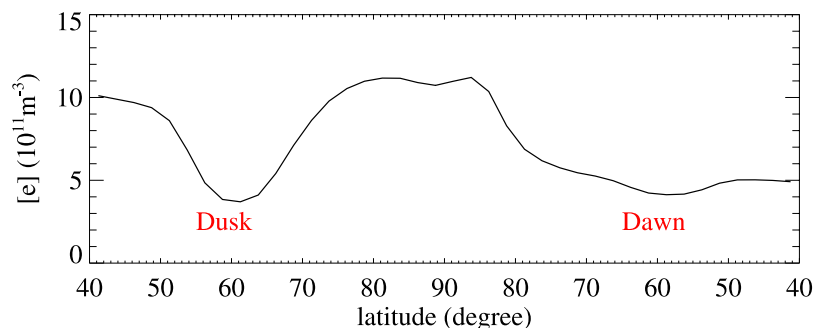

Figure 3. E-field enhanced time electron density profile along the satellite trajectory, which is close to the dawn-dusk meridional plane.
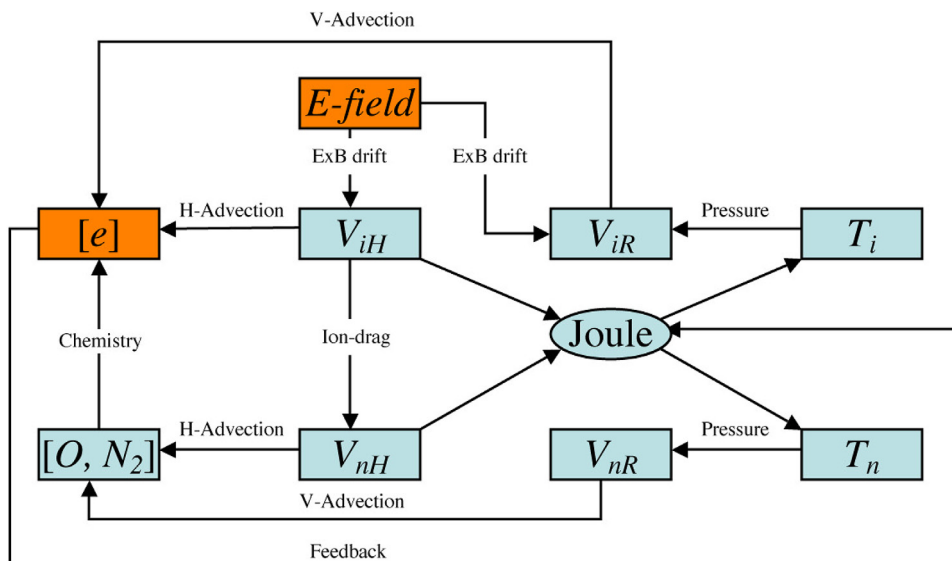
Figure 4. Diagram showing the main couplings in the polar region during the E-field enhanced time. "H-Advection" means horizontal advection and "V-Advection" means vertical advection. V_{iH} represents the horizontal ion velocity; V_{iR} represents the vertical ion velocity.

the $\mathbf{E} \times \mathbf{B}$ drift and the pressure gradient; and (3) chemical reactions, which are affected by the neutral advection, neutral composition, electron density and temperatures. In the next several subsections, the variations of NmF_2, hmF_2 and the electron density distribution are investigated, then the impact of the three processes described above is compared to identify the consequences of vertical circulation during the early stage of electric field enhancement.

3.1. NmF_2 and hmF_2 Variations

[12] Figure 5a shows the distribution of horizontal ion velocity and changes in the Joule heating at 1210, 1230 and 1300 UT. When the southward B_z rises to 20 nT, the magnitude of horizontal ion velocity can exceed 1200 m/s, and the Joule heating significantly increases in both the dusk and dawn sectors. Comparison between 1210 UT and 1300 UT shows that as a consequence of ramping up the neutral winds, the Joule heating is reduced even though the electric field remains constant, shown by Y. Deng and A. J. Ridley (Possible reasons for underestimating of joule heating in global modes: E-field variability, spatial resolution and vertical velocity, submitted to *Journal of Geophysical Research*, 2006).

[13] The definition of ionospheric positive and negative storm phases is based on the changes of NmF_2 or TEC [*Lu et al.*, 2001]. Therefore those changes are examined first. As shown in Figure 5b, there are strong increases of NmF_2 on the nightside of the polar cap, but relatively small changes at noon time. The troughs on both dusk and dawn sides are intensified, and also extend further in longitude with time. The region of the tongue coincides with the enhanced antisunward ion convection, which moves dayside high-density plasma into the polar cap. The regions of troughs coincide with the sunward ion convection, which advects the nightside low-density plasma into the dayside. These are consistent with *Schunk and Sojka* [1996] and *Crowley et al.* [1996].

[14] Interestingly, there is a negative island near noon between $70°$ and $80°$ at both 1210 and 1230 UT in Figure 5b. The altitude profiles of electron density at 1210 UT in both background and enhanced electric field cases are shown in Figure 6. While the hmF_2 increases 60 km when the electric field is enhanced, the NmF_2 is slightly reduced. As we know, normally when the F_2 layer moves to high altitudes, the chemical recombination rate decreases, and hence the electron density increases. In order to figure out the reason for this reduced electron density, we plot the changes of time integrated total source, horizontal advection source and vertical source (see the definition in the section 3.3) at 380 km altitude in Figure 7. This altitude is between the F_2 peaks in the background case and E-field enhanced case. It is clear that the integrated total source, which is equal to the change of electron density, is very similar to the integrated horizontal source. Both of them are kind of patchy poleward $70°$ and the negative islands are from the contribution of the horizontal advection source. The vertical convection source is smaller than the horizontal advection source at 380 km altitude, although vertical convection is more important at both 250 km and 450 km altitudes. This is because around 380 km altitude, the vertical density gradient is much smaller than that at 250 km and 450 km. Even though there is strong upward advection, its impact to the density is not as significant as at other locations.

[15] Figure 5c shows that the changes of calculated TEC have similar distributions as NmF_2. The amplitude change, approximately 15 TECU, is very close to the simulation results given by *Lu et al.* [2001], but an order of magnitude smaller than the observed TEC variations given by *Foster et al.* [2005]. This is because the changes in TEC are dependent on solar and geomagnetic activities. Using the *Burton et al.* [1975] equation, it is seen that a Bz of -20 nT (with a solar wind velocity of 400 km/s) will give a D_{st} of -40.5 nT in 1 hour, which is very close to the condition given by *Lu et al.* [2001]. However, in the work by *Foster et al.* [2005],
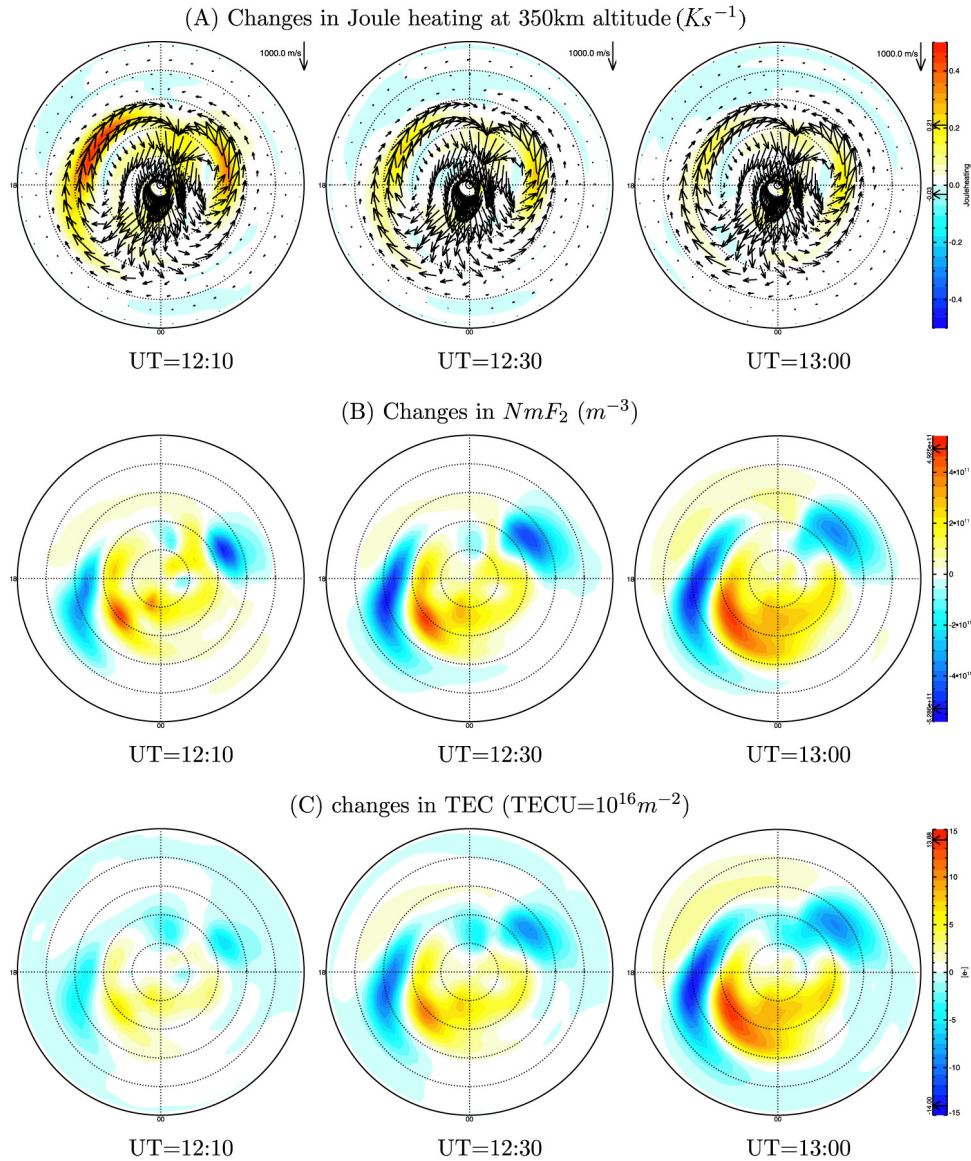
Figure 5. Snapshots of changes in (a) Joule heating, (b) NmF_2 and (c) TEC with respect to the background case at 1210, 1230 and 1300 UT. In Figure 5a the vectors show the horizontal ion convection and the color contours show the changes in Joule heating. In all of the figures, the outside rings are $40°$ latitude.

D_{st} is close to -500 nT and is an order of magnitude larger than the D_{st} in our study. So it is not a surprise that the TEC variation given by *Foster et al.* [2005] is much larger than the results presented in Figure 5c.

[16] It is notable that TEC is diminished while NmF_2 is enhanced at 1300 UT, noon and lat = 70°. The possible explanation is that the upward ion drift pushes hmF_2 to higher altitude, and hence increases NmF_2, as shown in Figure 8a. However, our calculated TEC is the height-integrated electron density from 100 km to 500 km. When NmF_2 moves higher, more electron density has been cut off by the upper boundary, artificially reducing the calculated TEC. *Lu et al.* [2001] mentioned that the topside electron density, above the upper boundary, could contribute 25% of the real TEC in the polar region. During super magnetic storms, the F_2 peak can move to above 500 km altitude

[Foster et al., 2005], and the topside contribution to TEC may be even larger than 50%.

[17] In the polar region, the magnetic field is almost vertical. Therefore the $\mathbf{E} \times \mathbf{B}$ drift is typically considered to be mostly horizontal. Nevertheless, Figure 9a shows that ion drifts can have a significant vertical component with large upward flow on the dayside and downward flow on the night side. The maximum velocity is close to 180 m/s, which is still relatively small compared with the horizontal component, but comparable with the vertical ion drift at mid and low latitudes. Although this result is a little bit of a surprise at first, it is very reasonable considering the change of geomagnetic dip angle with latitude and the significant convection electric field in the polar region. For example, in the auroral zone (66° latitude), the dip angle is close to 82°. In an enhanced electric field time when the magnitude of $\mathbf{E}$
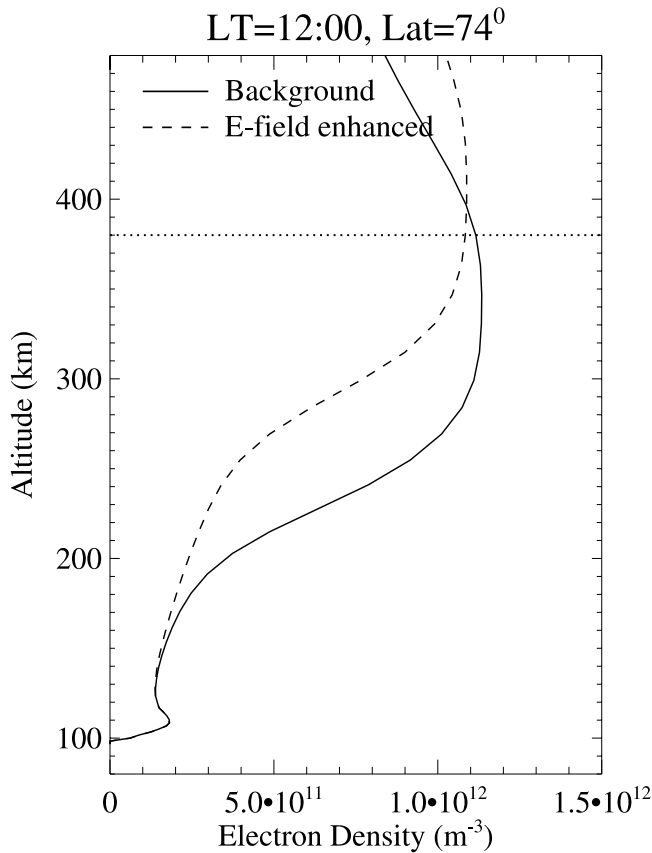
LT=12:00, Lat=74⁰

Figure 6. Altitude profile of electron density at 1210 UT in the position (LT = 1200, Latitude = 74°), which is marked in Figure 7a. The solid lines represents the profile in the background case, and the dashed line represents the profile in the E-field enhanced case. The dotted line marks the altitude (380 km) in Figure 7.

$\times$ **B** drift is more than 1000 m/s, this 8° decrease of the dip angle can produce a 100 m/s vertical ion drift. On the dayside, the eastward electric field and the northward geomagnetic field generate the upward **E** $\times$ **B** drift. While

on the nightside, the **E** $\times$ **B** drift is downward in response to the westward E-field.

[18] According to the dominance of **E** $\times$ **B** drift on the ion velocity at high latitudes [*Deng and Ridley*, 2006], changes in V_{iR}, as shown in Figure 9b, are similar to the variations in vertical **E** $\times$ **B** drift, especially at the beginning of the E-field enhanced time. However, the magnitude of V_{iR} decreases with the time when the vertical **E** $\times$ **B** drift does not change. The reason is that when the plasma is transported vertically, the modified pressure gradient gradually reduces the vertical ion drift. Figure 9 shows a rough correlation between V_{iR} and hmF_2: where V_{iR} is upward, hmF_2 ascends; where V_{iR} is downward, hmF_2 descends. Note that hmF_2 calculated in this study is the altitude of maximum electron density within the model. In the background case, the F_2 peak can be missing during the night time because of a lack of coupling between the ionosphere and a plasmasphere in GITM. Hence the altitude of maximum electron density within the model at night in the midlatitudes may be at the top boundary of the model. During the enhanced electric field, V_{iR} is downward at night, which produces a F_2 peak around 400 km altitude. Therefore the calculated change of hmF_2, -100 km, may not be very precise and different from the observations in the night sector.

3.2. N_e Distribution Variations

[19] While NmF_2 and hmF_2 are very important parameters for the ionosphere, they only show the variation about the F_2 peak. In order to better understand the changes in electron density, we investigate the changes of altitude distribution at two positions: (1) lat = 66°, noon and (2) lat = 66°, midnight. As shown in Figure 8, the F_2 layer moves upward at noon and augments at midnight. It is clear that the response of the electron density to changes in the electric field is spatial-dependent. Even if the changes of F_2 peak are the same, the topside and bottomside of the F_2 layer could be different. Therefore we examine the spatial distribution of the perturbations in the thermosphere and ionosphere at two specific altitudes: 250 km (below the F_2 peak) and 450 km (above the F_2 peak).

Source changes at 380km altitude, 12:10UT

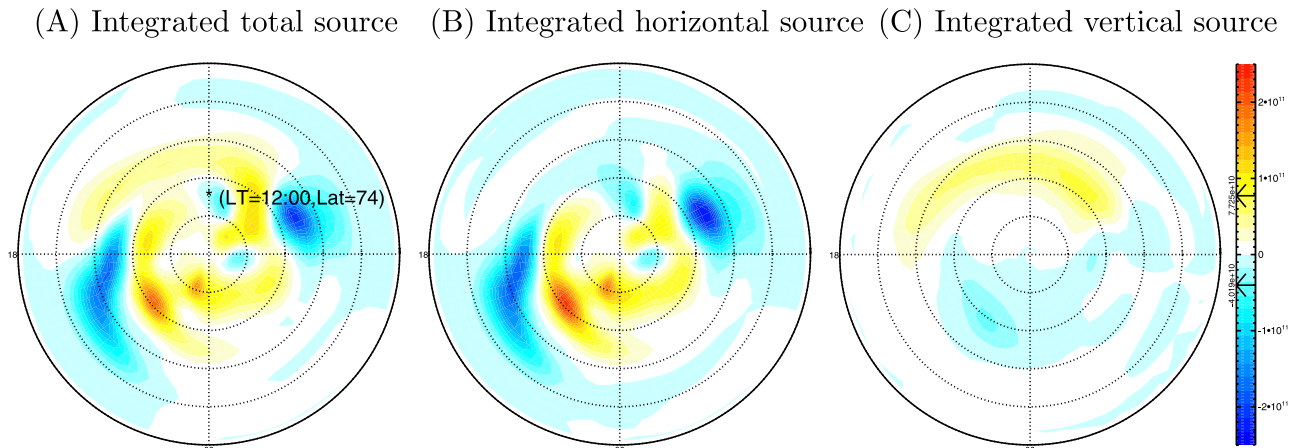(A) Integrated total source   (B) Integrated horizontal source   (C) Integrated vertical source

Figure 7. Snapshots of changes in the time-integrated (a) total source, (b) horizontal advection source and (c) vertical advection source at 380 km altitude 1210 UT with respect to the background case.
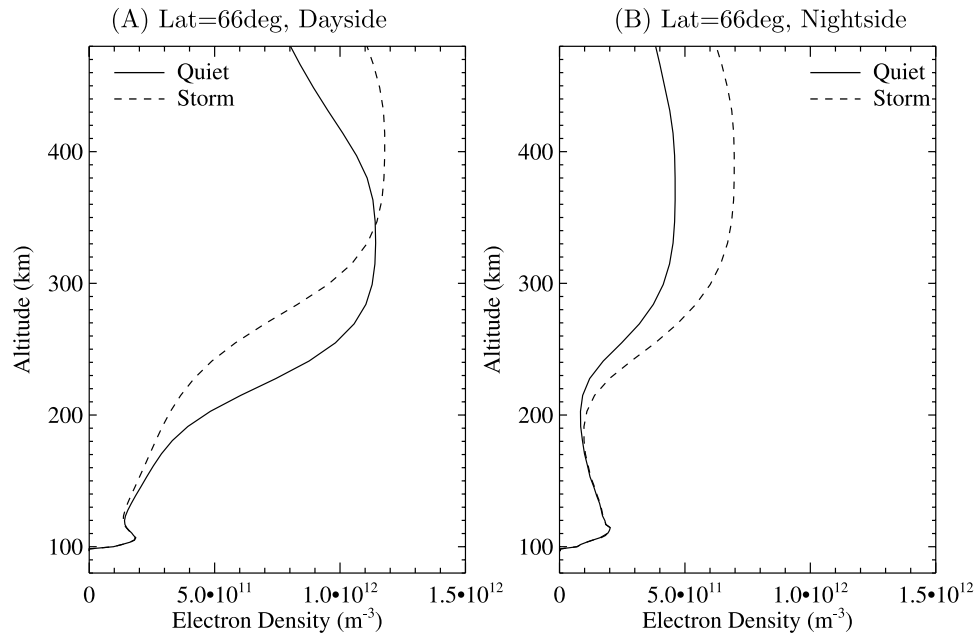
Figure 8. Altitude profile of electron density at 1300 UT (a) close to noon and (b) close to midnight. The solid lines represent the profile in the background case, and the dashed lines represent the profile in the E-field enhanced case.

[20] Figure 10 shows that at 250 km altitude, the electron density decreases on the dayside where ion drift has an upward component, and increases on the nightside where ion drift has a downward component. At 450 km altitude and 1210 UT, the electron density increases on the dayside and decreases on the nightside equatorward of 70°. This distribution seems to have some correlation with the change of vertical ion drift, which is upward on the dayside and downward on the nightside. *Schunk and Nagy* [2000] also documented that the upward ion drift could lead to an increase on the topside electron density, and the reverse is true for a downward ion drift. After 1 hour (1300 UT), there are obvious tongues of ionization in the polar cap and troughs in the lower latitudes, which is related to the horizontal convection. We also show the change percentage of electron density with respect to the background case at two altitudes in Figure 11, which represents significant ionospheric disturbance. For example, the increasing percentage of electron density can be more than 300% at 250 km and almost 100% at 450 km. The absolute value of change percentages on the dayside is smaller than that on the nightside, which is due to the magnitude difference of electron density between dayside and nightside in the background case.

[21] On the basis of these results, we propose a vertical circulation, shown in Figure 12, in the noon-midnight meridional plane during the early stage of E-field enhancement in addition to the widely accepted horizontal two-cell convection. On the dayside, when the vertical convection moves the F_2 layer upward, the bottomside electron density at a fixed altitude (e.g., 250 km) decreases because this altitude becomes far from the F_2 peak. The topside electron density increases because of the F_2 layer shift. Then, the horizontal antisunward advection moves the electron den-

sity from dayside to nightside. Meanwhile, on the night side, the downward vertical convection pushes the plasma from the high altitudes to the low altitudes. On the bottom side, chemistry, which produces electrons on the dayside through solar EUV ionization and recombines electrons and ions on the nightside, balances the advection.

[22] The O/N_2 ratio is a widely used parameter to present the neutral influence to the electron density. Hence the temporal variation of the O/N_2 ratio is also examined. Figure 13 shows that at 1210 UT, the O/N_2 ratio is negative and has a similar distribution to the Joule heating (Figure 5a), which indicates that the Joule heating does lift the neutral atmosphere up and is dominant at the beginning of the E-field enhanced time. The snapshot at 1300 UT shows that the distribution is twisted as the consequence of the increased horizontal convection. However, there is no clear correlation between the changes in electron density and the changes in the O/N_2 ratio, and the results are different from previous ones [*Fuller-Rowell et al.*, 1997; *Lu et al.*, 2001]. This discrepancy is related to the timescale difference. The timescale used in this study is only 1 hour, which is much shorter than that in simulations of *Fuller-Rowell et al.* [1997] and *Lu et al.* [2001], who examine 24 hours timescale. The O/N_2 ratio is proportional to the electron density only when the chemistry is dominant and the system is around chemical equilibrium. The first hour of E-field enhanced time is far from equilibrium, and hence the correlation between the O/N_2 ratio and the electron density is poor. Later, when the system is closer to equilibrium, the O/N_2 ratio is still an effective tracer of the electron density.

[23] While the changes of the O/N_2 ratio at 450 km are larger than that at 250 km, the changes in the time-integrated chemical source at 450 km (Figure 15a) are much smaller than that at 250 km (Figure 14a). This is because the
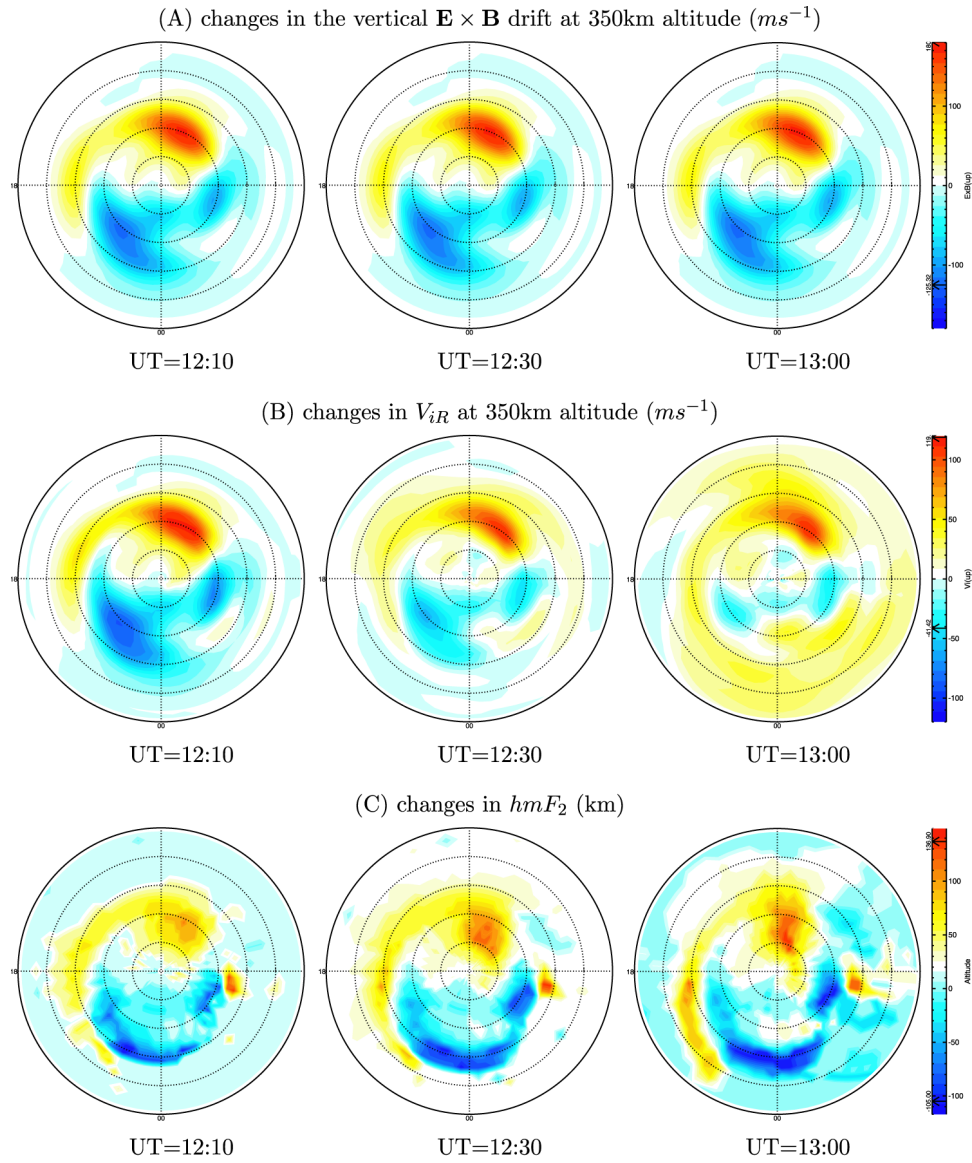
(A) changes in the vertical $\mathbf{E} \times \mathbf{B}$ drift at 350km altitude (ms^{-1})

UT=12:10   UT=12:30   UT=13:00

(B) changes in V_{iR} at 350km altitude (ms^{-1})

UT=12:10   UT=12:30   UT=13:00

(C) changes in hmF_2 (km)

UT=12:10   UT=12:30   UT=13:00

Figure 9. Snapshots of changes in (a) vertical $\mathbf{E} \times \mathbf{B}$ drift, (b) V_{iR} and (c) hmF_2 with respect to the background case at 1200, 1230 and 1300 UT.

O/N_2 ratio is not the only factor affecting the chemical source. We roughly define the chemical source like

$$S_c = -k_1[N_2][e] + k_2[O],$$

where k_1 and k_2 are chemical reaction rates. So the first term on the right hand side is the loss term and the second term is the source term. We reform the equation and get

$$S_c = \left(-k_1[e] + k_2\frac{[O]}{[N_2]}\right)[N_2].$$

While the O/N_2 ratio is larger at 450 km, the N_2 density exponentially decreases with the altitude and is two orders of magnitude smaller at 450 km than that at 250 km. So the chemical source is significant at 250 km altitude but negligible at 450 km altitude.

[24] At 450 km altitude and 1300 UT, there is an O/N_2 ratio increase region on the dawnside, which is actually a low-density cell [*Crowley et al.*, 1996; *Schoendorf et al.*, 1996a, 1996b]. Both N_2 and O contents decrease at this place, but there is a larger decrease of N_2. Therefore the O/N_2 ratio rises.

3.3. Comparison of Different Sources

[25] The vertical circulation during the early stage of E-field enhancement, as discussed in section 3.2, is related to 3 sources: vertical advection, horizontal advection and chemistry. In order to show that this circulation works, the relative importance of these sources is investigated. From the continuity equation, the change of electron density is

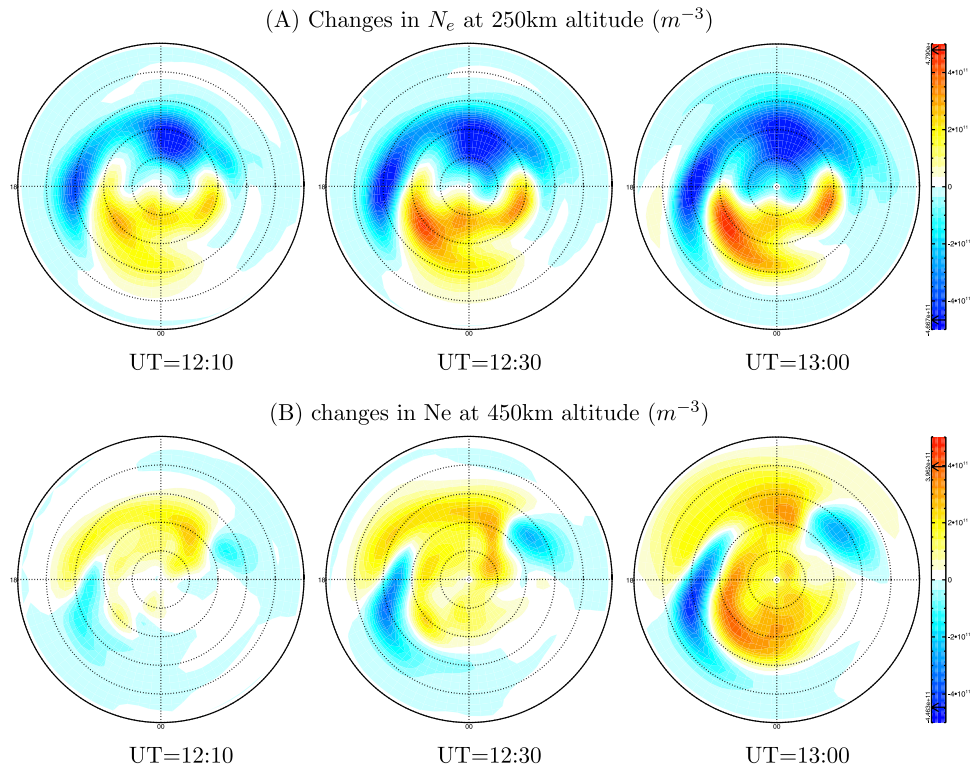$$\frac{\partial n}{\partial t} = -\nabla\cdot(n\mathbf{u}) + S_C = S_H + S_R + S_C \qquad (1)$$

(A) Changes in N_e at 250km altitude (m^{-3})

UT=12:10   UT=12:30   UT=13:00

(B) changes in Ne at 450km altitude (m^{-3})

UT=12:10   UT=12:30   UT=13:00

Figure 10. Snapshots of changes in electron density (a) at 250 km altitude and (b) at 450 km altitude with respect to the background case.

(A) Change percentage in N_e at 250km altitude (%)

UT=12:10   UT=12:30   UT=13:00

(B) change percentage in Ne at 450km altitude (%)

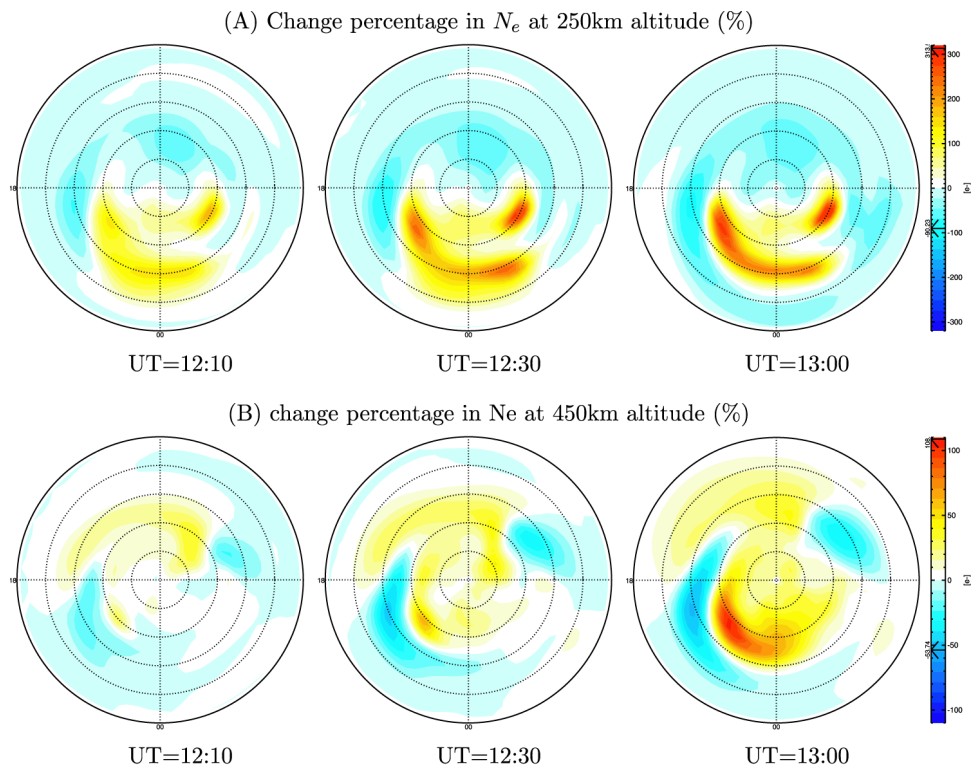UT=12:10   UT=12:30   UT=13:00

Figure 11. Snapshots of electron density change percentage (a) at 250 km altitude and (b) at 450 km altitude with respect to the background case. The legend is from -320 to 320 in Figure 11a and from -110 to 110 in Figure 11b.
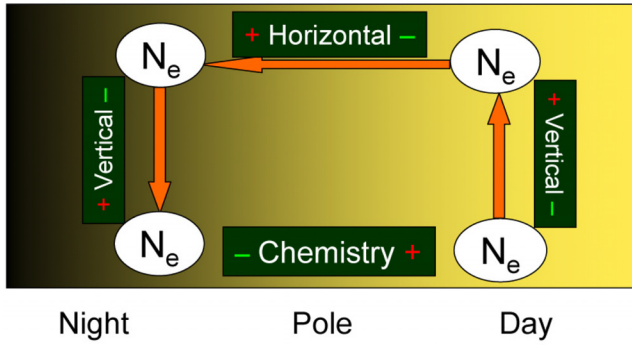
Figure 12. Vertical circulation in the noon-midnight plane during the early stage of E-field enhancement, which is related to three mechanisms: vertical advection, horizontal advection and chemistry. The green minus sign means negative effect, and the red plus sign means positive effect. The yellow arrow indicates the direction of the advection.

where $S_H = -\nabla_H \cdot (n\mathbf{u})$, or horizontal advection source; $S_R = -\nabla_R \cdot (n\mathbf{u})$, or vertical advection source and S_C is the chemical reaction source. We define the enhanced E-field caused by changes in electron density and sources as: Δn, ΔS_H, ΔS_R, ΔS_C, where Δ means the difference between the E-field enhanced case and background case values. So the continuity equation for the E-field enhanced time is

$$\frac{\partial(n + \Delta n)}{\partial t} = S_H + \Delta S_H + S_R + \Delta S_R + S_C + \Delta S_C. \quad (2)$$

Subtracting equation (2) from equation (1), we get

$$\frac{\partial \Delta n}{\partial t} = \Delta S_H + \Delta S_R + \Delta S_C. \quad (3)$$

Integrating both sides, the change in electron density is

$$\Delta n = \int_{t_0}^{t} \Delta S_H dt + \int_{t_0}^{t} \Delta S_R dt + \int_{t_0}^{t} \Delta S_C dt, \quad (4)$$

where t_0 = 1200 UT.

[26] Equation (4) shows that the change in electron density is an integrated effect of source difference over the E-field enhanced period. In order to examine the relative importance of various mechanisms, we calculate the changes in time-integrated chemical reaction, horizontal advection and vertical advection sources. Figure 14 shows that at 250 km altitude, these three sources are of the same order(10^{12} m^{-3}). At 1210 UT, the vertical advection source has stronger contributions than the other two. In response to the vertical advection, the chemical sources attempt to restore an equilibrium; therefore they are opposite and slightly time-lagged to the vertical advection. The horizontal advection also modifies the electron density change pattern, with a negative contribution in the polar cap in response to the reduced electron density transported from the dayside.

[27] Figure 15 shows that at 450 km altitude, the effect of chemical source is negligible, and the contributions of horizontal advection and vertical advection are comparable. The horizontal advection increases electron density in the
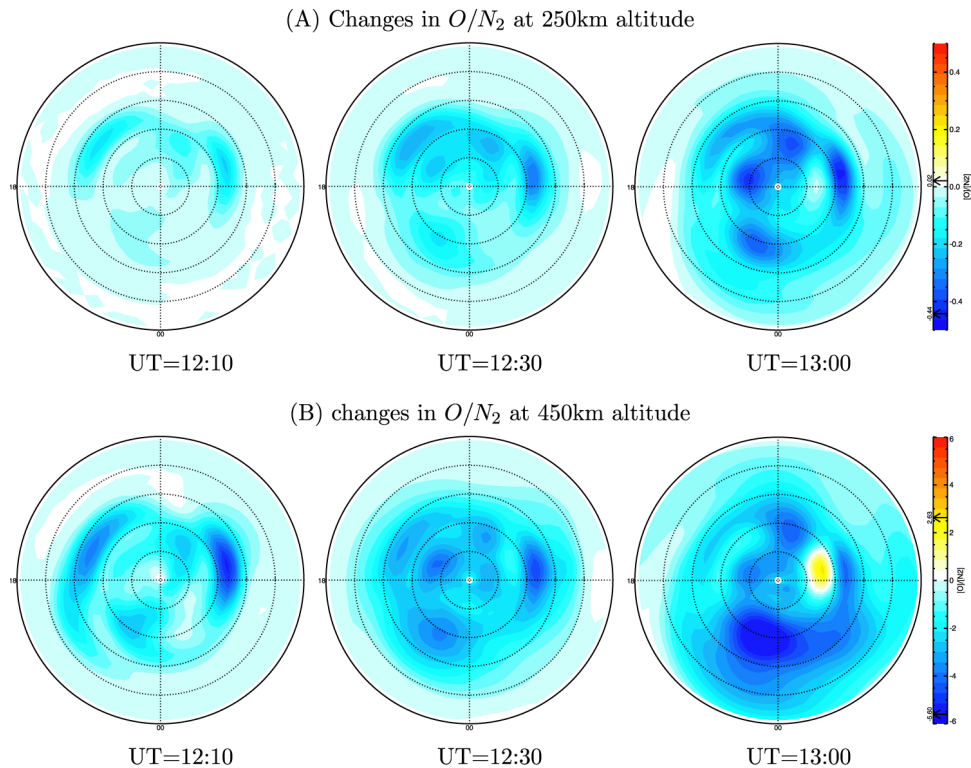

Figure 13. Snapshots of changes in O/N_2 ratio (a) at 250 km altitude and (b) at 450 km altitude with respect to the background case.

(A) Changes in time-integrated chemical source at 250km (m^{-3})

UT=12:10   UT=12:30   UT=13:00

(B) Changes in time-integrated horizontal advection source at 250km (m^{-3})

UT=12:10   UT=12:30   UT=13:00

(C) Changes in time-integrated vertical advection source at 250km (m^{-3})
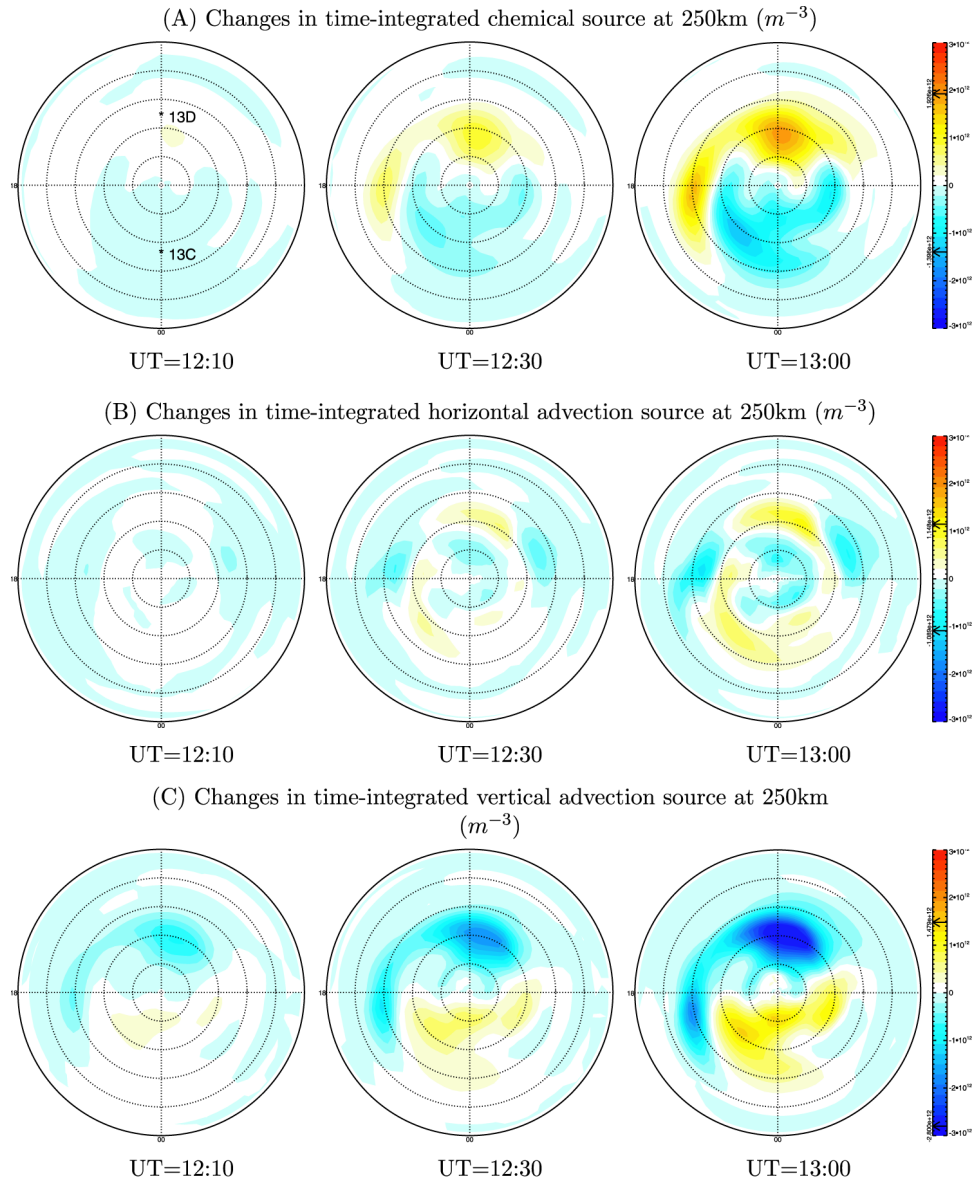

UT=12:10   UT=12:30   UT=13:00

Figure 14. Snapshots of changes in the time-integrated (a) chemical source, (b) horizontal advection source and (c) vertical advection source at 250 km altitude with respect to the background case. "13C" and "13D" mark the positions of Figures 16c and 16d.

polar cap and decreases it at the lower latitudes. Meanwhile, the vertical advection raises the dayside electron density and reduces the nightside electron density.

[28] The relative importance of different mechanisms is dependent on the position. Therefore we investigate the time variations of changes in time-integrated sources at four specific places: (1) lon = 180°, lat = 66°, alt = 450 km; (2) lon = 0°, lat = 66°, alt = 450 km; (3) lon = 180°, lat = 66°, alt = 250 km; (4) lon = 0°, lat = 66°, alt = 250 km. Locations 1 and 3 are close to midnight local time, while locations 2 and 4 are close to noon. Figures 16c and 6d show that at 250 km altitude, the vertical advection acts faster than the other two sources, so the changes in electron density follow it. Then, the vertical advection is balanced by the chemical source and horizontal advection. According to the opposite directions of V_{iR} between noon and midnight,

chemical and total sources in Figure 16c are reversed with respect to Figure 16d. On the topside (450 km), the major balance is between vertical advection and horizontal advection, and the chemical source is negligible. The electron density gradient is opposite between the topside and the bottomside of the F_2 layer. With the same sign vertical velocity at both altitudes, the contribution of vertical advection to the electron density will then be opposite above and below the F_2 peak. Surprisingly, both the bottomside and the topside cases show the dominant role of vertical advection, which has been ignored in the polar region for most studies. The total changes of the source, which are equal to the changes of electron density, follow the changes of time-integrated vertical advection in all of the cases except in Figure 16a, which shows the prominent effect of the horizontal advection.
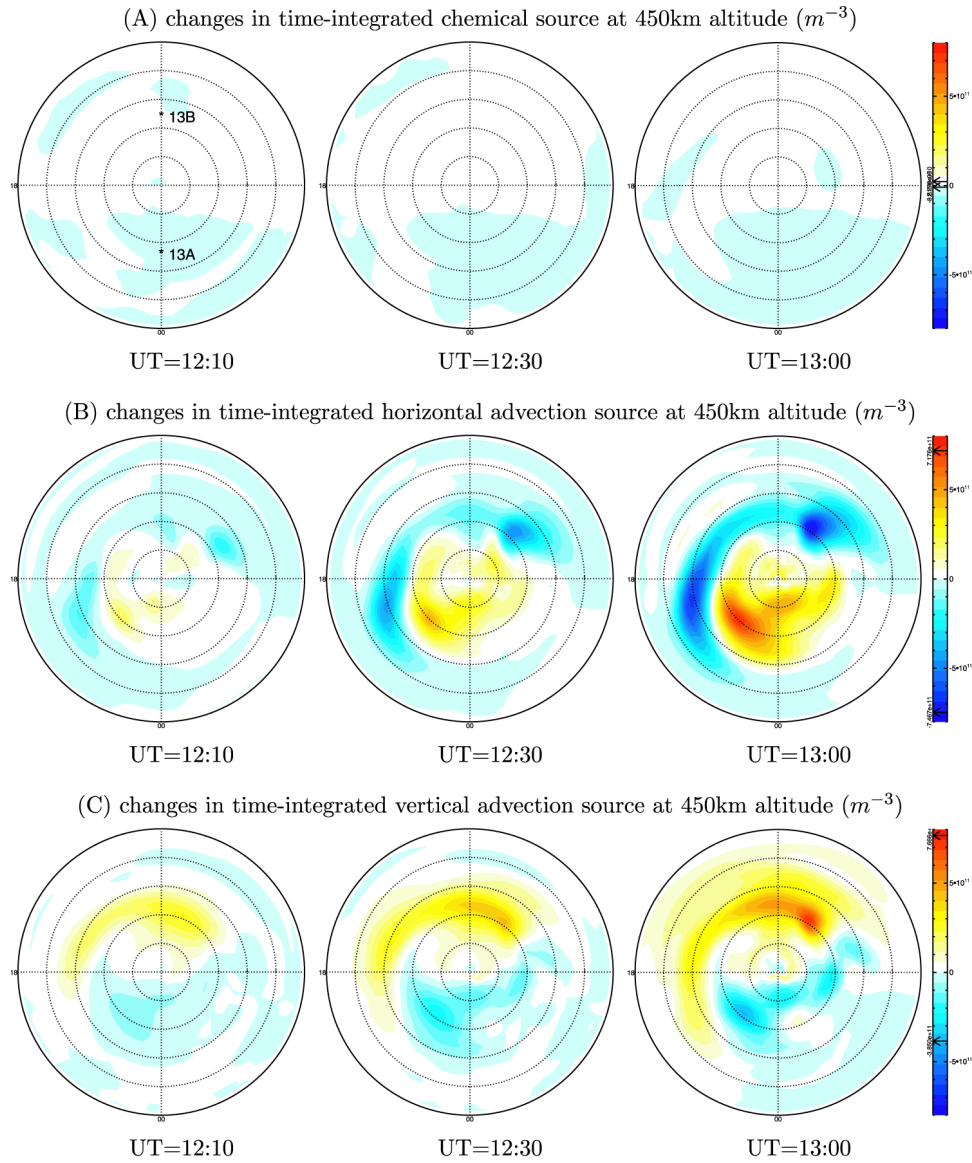
(A) changes in time-integrated chemical source at 450km altitude (m^{-3})

(B) changes in time-integrated horizontal advection source at 450km altitude (m^{-3})

(C) changes in time-integrated vertical advection source at 450km altitude (m^{-3})

Figure 15. Snapshots of changes in the time-integrated (a) chemical source, (b) horizontal advection source and (c) vertical advection source at 450 km altitude with respect to the background case. "13A" and "13B" mark the positions of Figures 16a and 16b.

[29] These results are the same as what the vertical circulation indicates in Figure 12. So it is safe to say that the simulation and the circulation are qualitatively consistent during the early stage of E-field enhancement. According to the vertical circulation, a significant source of the tongue ionization is not only the plasma on the dayside from lower latitudes, which has been widely accepted, but also lower altitudes. The case we have studied is highly idealized. The quantitative results may be different in the super magnetic storms. Examination of the dependence of relative importance between the horizontal convection and vertical advection on the solar and geomagnetic activities would be very interesting and definitely a part of our future work.

[30] As mentioned in section 2, the timescale we have investigated is the first hour after the electric field has been enhanced, which is much shorter than the typical storm time, like 12 or 24 hours. In order to show the significance of vertical advection during longer time scale, we run GITM for 6 hours with the enhanced E-field and investigate the relative importance of different sources at that moment. As shown in Figure 17, because of the turbulence of the thermosphere and ionosphere after the E-field enhancement, the distributions of sources are patchy. After the ions are shifted vertically, both the pressure gradient and vertical ion velocity are changed. Hence the vertical circulation is not well organized as in the first hour. However, the contribution of the vertical advection to the electron density is still significant compared with the other two sources at both altitudes.

3.4. Vertical E × B Drift in APEX Coordinates

[31] In our previous section, GITM is run with a simple dipole magnetic field, which is highly idealized with no universal time (i.e., longitudinal) dependence. In order to
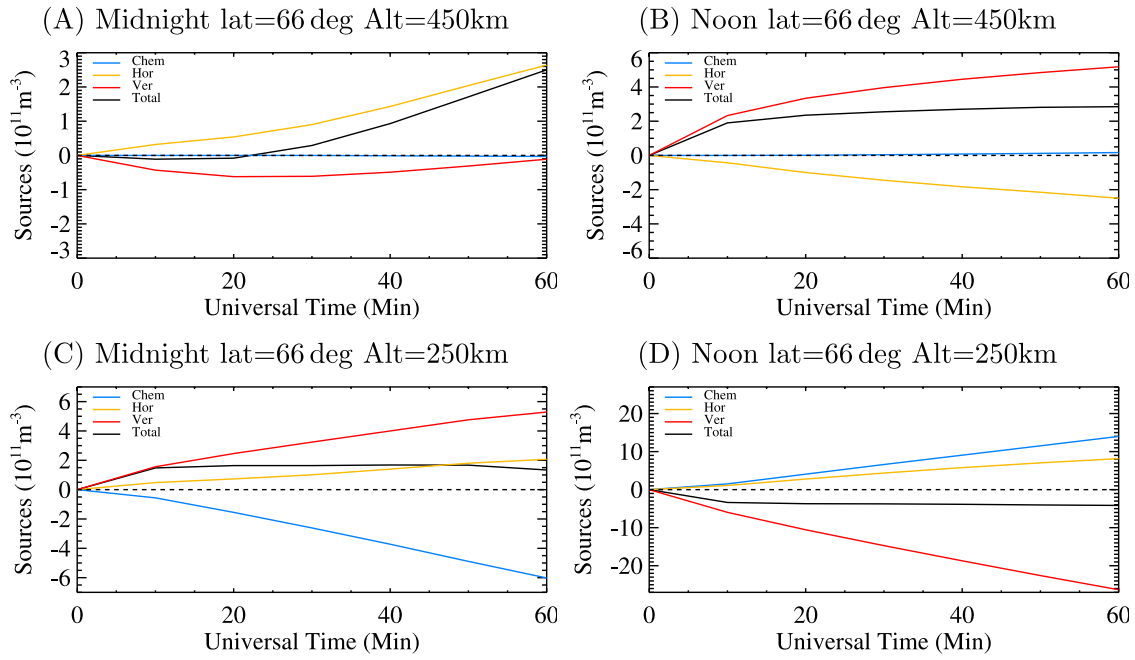
Figure 16. Time variation of the time-integrated different sources between E-field enhanced case and background case, starting from 1200 UT at (a and b) 450 km altitude and (c and d) 250 km altitude. Figures 16a and 16c are close to midnight; Figures 16b and 16d are close to noon. The positions are indicated in Figures 14 and 15.

examine more realistic cases, we have run GITM with internal geophysical reference field (IGRF) in the APEX coordinate system [*Richmond*, 1995]. As shown in Figure 18, because of the dislocation of the magnetic pole

and the geographic pole, the distribution of the magnetic dip angle rotates around the geographic pole throughout the day. The changes of the geomagnetic tilt angle affect the reconnection between the solar wind magnetic field and the
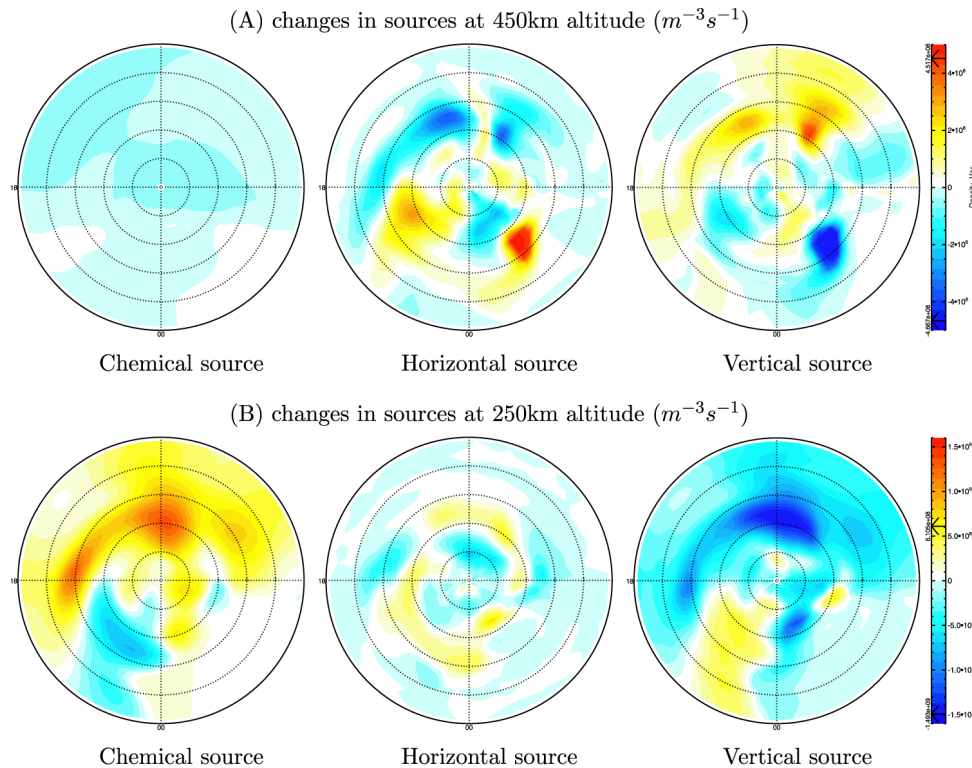

Figure 17. Snapshots of changes in chemical, horizontal and vertical sources after 6-hour E-field enhancements (UT = 1800) at (a) 450 km and (b) 250 km altitudes with respect to the background case.
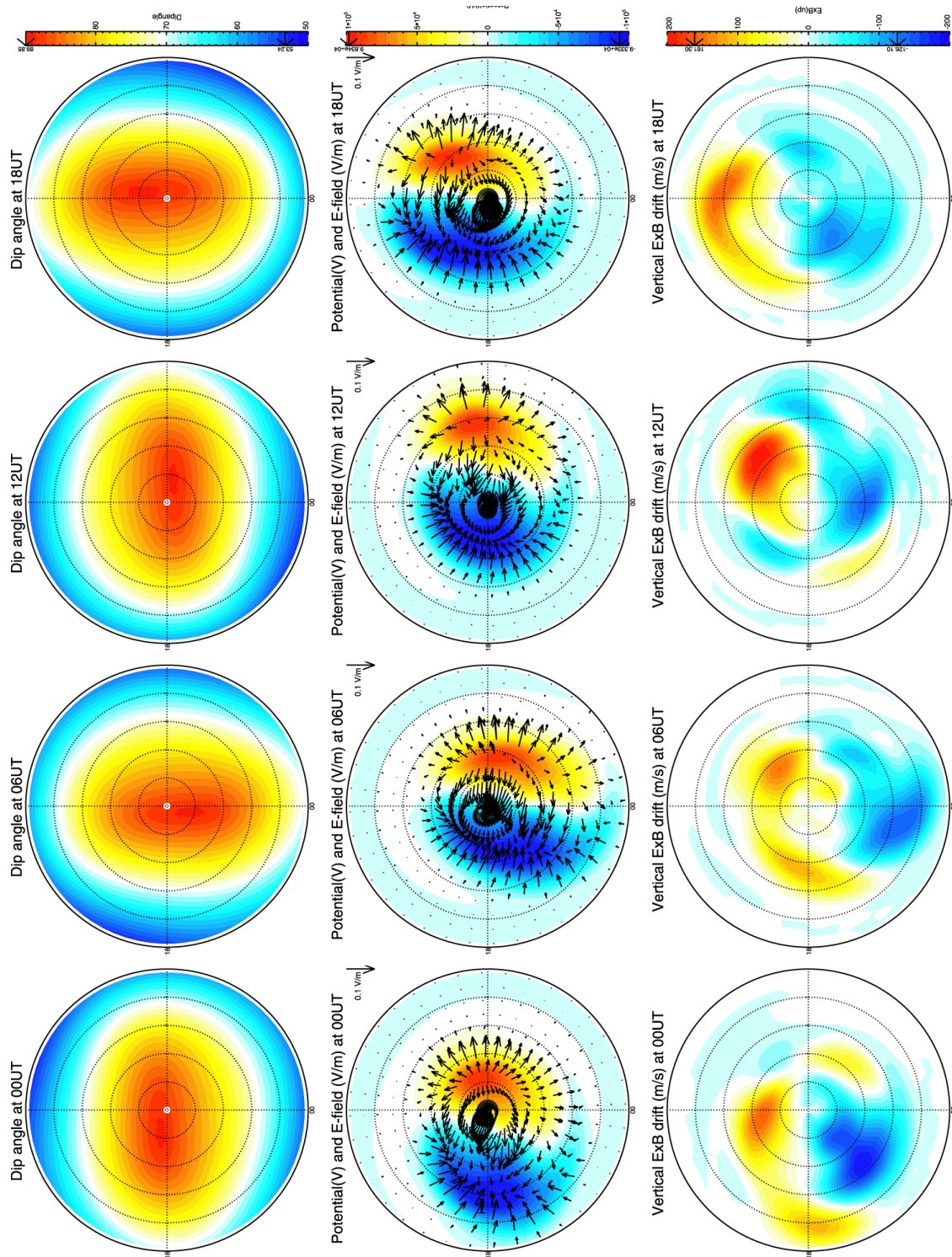
Figure 18. Snapshots of changes in (top) magnetic dip angle, (middle) polar cap potential and (bottom) vertical component of $\mathbf{E} \times \mathbf{B}$ drift at four universal times (0000 UT, 0600 UT, 1200 UT and 1800 UT) when GITM is run with the IGRF magnetic field in the APEX coordinate system. In Figure 18 (middle), the vectors show the electric field.

geomagnetic field at the magnetopause, and hence change the polar cap potential, as shown in the middle column of Figure 14 [see *Weimer*, 1996]. The maximum and minimum potential positions shift according to the change of the geomagnetic pole. For example, at 0000 UT, when the geomagnetic pole is duskward of the geographic pole, the potential extrema relatively move to the dusk direction. Similar changes happen at the other times. In response to the variation of both the magnetic field and the electric field, the vertical $\mathbf{E} \times \mathbf{B}$ drift distribution changes significantly. The upward $\mathbf{E} \times \mathbf{B}$ drift varies from triple peaks (at 0000 UT) to a single peak (at 1800 UT) and the maximum position changes from $75°$ to $60°$. These changes may cause significant variability in the dynamics of patches and tongues of ionization caused by dayside vertical flows. Although the vertical $\mathbf{E} \times \mathbf{B}$ drift in Apex coordinates is more complex than that in Figure 6a, the main characteristics are the same. Overall, the vertical drift is upward on the dayside and downward on the nightside. The maximum magnitude of vertical drift is between 100 and 200 m/s. Therefore the vertical circulation is significant for the electron density distribution during the early stage of E-field enhancement, while the configuration of the circulation is complex and variable in reality.

4. Summary and Conclusion

[32] We use GITM to investigate the ionospheric variation at the high latitudes and its relationship to horizontal advection, vertical advection and chemistry during the first hour of electric field enhancement. The analysis has led to the following conclusions:

[33] In response to the enhanced convection Electrical field, both the convection velocity and Joule heating increase dramatically. The changes in NmF_2 show that a tongue of ionization extends across the polar cap and the troughs stretch longitudinally. The changes of calculated total electron content (TEC) can reach 15 TECU and have a similar pattern to the changes of NmF_2.

[34] As a consequence of the changes in the $\mathbf{E} \times \mathbf{B}$ drift, the changes in the vertical ion drift can be larger than 100 m/s, upward on the dayside and downward on the nightside. Vertical transport of plasma modifies the pressure gradient, which gradually reduces the vertical ion drift. Approximately, hmF_2 ascends where V_{iR} is upward and descends where V_{iR} is downward.

[35] In general, the response of the ionosphere to the enhanced electric field is that the F_2 layer moves upward on the dayside and augments on the nightside. Below the F_2 peak (250 km altitude), the region of decreased electron density coincides with the upward V_{iR} on the dayside, and the reverse is true on the nightside. Above the F_2 peak (450 km altitude), the features related with both horizontal convection and vertical advection are present. The vertical ion drift sets up a vertical circulation in the noon-midnight meridional plane during the early stage of E-field enhancement in addition to the widely accepted horizontal two cell convection. According to the circulation, the significant sources of the tongue of ionization are not only the plasma from the lower latitudes, but also from the low altitudes on the dayside. While the vertical circulation is not well

organized after 6-hour E-field enhancement, the contribution of vertical ion convection is still significant.

[36] Although the vertical $\mathbf{E} \times \mathbf{B}$ drift in Apex coordinates is more complex and variable than that in a simple dipole magnetic field, the main characteristics are the same, which indicate the significance of the vertical circulation for the electron density distribution in reality during the early stage of E-field enhancement.

[37] The Joule heating drives upwelling of the atmosphere and modifies the O/N_2 ratio. Meanwhile, the enhanced neutral advection twists the O/N_2 ratio pattern a little bit. However, the changes in the O/N_2 ratio have relatively poor correlation with the variation of electron density during the first hour of E-field enhanced time.

References

Banks, P. M. (1977), Observations of Joule and particle heating in the auroral zone, *J. Atmos. Terr. Phys.*, *39*, 179.

Bauske, R., and G. W. Prölss (1997), Modeling the ionospheric response to traveling atmospheric disturbances, *J. Geophys. Res.*, *102*, 14,555.

Buonsanto, M. J. (1999), Ionospheric storms—A review, *Space Sci. Rev.*, *88*, 563.

Burns, A. G., T. L. Killeen, and R. G. Roble (1991), A simulation of thermospheric composition changes during an impulsive storm, *J. Geophys. Res.*, *96*, 14,153.

Burton, R. K., R. L. McPherron, and C. T. Russell (1975), An empirical relationship between interplanetary conditions and Dst, *J. Geophys. Res.*, *80*, 4204.

Crowley, G., J. Schoendorf, R. G. Roble, and F. A. Marcos (1996), Cellular structures in the high-latitude thermosphere, *J. Geophys. Res.*, *101*, 211.

Deng, Y., and A. J. Ridley (2006), Dependence of neutral winds on convection E-field, solar EUV and auroral particle precipitation at high latitudes, *J. Geophys. Res.*, doi:10.1029/2005JA011368, in press.

Field, P. R., H. Rishbeth, R. J. Moffett, D. W. Idenden, T. J. Fuller-Rowell, G. H. Millward, and A. D. Aylward (1998), Modelling composition changes in F-layer storm, *J. Atmos. Sol. Terr. Phys.*, *60*, 523.

Foster, J. C., J. M. Holt, R. G. Musgrove, and D. S. Evans (1986), Ionospheric convection associated with discrete levels of particle precipitation, *Geophys. Res. Lett.*, *13*, 656.

Foster, J. C., S. Cummer, and U. S. Inan (1998), Midlatitude particle and electric field elffects at the onset of the November 1993 geomagnetic storm, *J. Geophys. Res.*, *103*, 26,359.

Foster, J. C., et al. (2005), Multiradar observations of the polar tongue of ionization, *J. Geophys. Res.*, *110*, A09S31, doi:10.1029/2004JA010928.

Fuller-Rowell, T. J., and D. Evans (1987), Height-integrated Pedersen and Hall conductivity patterns inferred from TIROS−NOAA satellite data, *J. Geophys. Res.*, *92*, 7606.

Fuller-Rowell, T. J., M. V. Codrescu, R. J. Moffett, and S. Quegan (1994), Response of the thermosphere and ionosphere to geomagnetic storms, *J. Geophys. Res.*, *99*, 3893.

Fuller-Rowell, T. J., M. V. Codrescu, R. G. Roble, and A. D. Richmond (1997), How does the thermosphere and ionosphere react to a geomagnetic storm?, in *Magnetic Storms*, *Geophys. Monogr. Ser.*, vol. 98, edited by B. T. Tsurutani et al., p. 203, AGU, Washington, D. C.

Hajj, G. A., R. Ibanez-Meier, E. R. Kursinski, and L. J. Romans (1994), Imaging the ionosphere with the Global Positioning System, *Int. J. Imaging Syst. Technol.*, *5*, 174.

Huang, C., J. C. Foster, L. P. Goncharenko, P. J. Erickson, W. Rideout, and A. J. Coster (2005), A strong positive phase of ionospheric storms observed by the Millstone Hill incoherent scatter radar and global GPS network, *J. Geophys. Res.*, *110*, A06303, doi:10.1029/2004JA010865.

Knipp, D. J., et al. (1989), Electrodynamic patterns for September 19, 1984, *J. Geophys. Res.*, *94*, 16,913.

Lu, G., A. D. Richmond, R. G. Roble, and B. A. Emery (2001), Coexistence of ionospheric positive and negative storm phases under northern winter conditions: A case study, *J. Geophys. Res.*, *106*, 24,493.

Maeda, S., T. J. Fuller-Rowell, and D. S. Evans (1989), Zonally averaged dynamical and compositional response of the thermosphere to auroral activity during September 18−24, 1984, *J. Geophys. Res.*, *94*, 16,869.

Mitchell, C. N., and P. S. J. Spencer (2003), A three-dimensional time-dependent algorithm for ionospheric imaging using GPS, *Ann. Geophys.*, *46*(4), 687.

Pavlov, A. V., and J. C. Foster (2001), Model/data comparison of F region ionospheric perturbation over Millstone Hill during the severe geomagnetic storm of July 15–16, 2000, *J. Geophys. Res.*, *106*, 29,051.

Prölss, G. W. (1980), Magnetic storm associated perturbations of the upper atmosphere: Recent results obtained by satellite-borne gas analyzers, *Rev. Geophys.*, *18*, 183.

Prölss, G. W. (1987), Storm-induced changes in the thermospheric composition at middle latitudes, *Planet. Space Sci.*, *35*, 807.

Prölss, G. W. (1993), On explaining the local time variation of ionospheric storm effects, *Ann. Geophys.*, *11*, 1.

Prölss, G. W. (1997), Magnetic strom associated perturbations of the upper atmosphere, in *Magnetic Storms*, *Geophys. Monogr. Ser.*, vol. 98, edited by B. T. Tsurutani et al., p. 227, AGU, Washington, D. C.

Prölss, G. W., L. H. Brace, H. G. Mayr, G. R. Carignan, T. L. Killeen, and J. A. Klobuchar (1991), Ionospheric storm effects at subauroral latitudes: A case study, *J. Geophys. Res.*, *96*, 1275.

Richards, P. G., and D. G. Torr (1986), A factor of 2 reduction in theoretical F_2 peak electron density due to enhanced vibrationally excitation of N_2 in summer at solar maximum, *J. Geophys. Res.*, *91*, 11,331.

Richmond, A. D. (1995), Ionospheric electrodynamics using magnetic apex coordinates, *J. Geomagn. Geoelectr.*, *47*, 191.

Ridley, A. J. (2000), Estimation of the uncertainty in timing the relationship between magnetospheric and solar wind processes, *J. Atmos. Sol. Terr. Phys.*, *62*, 757.

Ridley, A. J., C. R. Clauer, G. Lu, and V. O. Papitashvili (1997), Ionospheric convection during nonsteady interplanetary magnetic field conditions, *J. Geophys. Res.*, *102*, 14,563.

Ridley, A. J., Y. Deng, and G. Toth (2006), The global ionosphere-thermosphere model, *J. Atmos. Sol. Terr. Phys.*, *68*, 839.

Rishbeth, H., T. J. Fuller-Rowell, and A. D. Rodger (1987), F-layer storms and thermospheric composition, *Phys. Scr.*, *36*, 327.

Schoendorf, J., G. Crowley, and R. G. Roble (1996a), Neutral density cells in the high latitude thermosphere—2. Mechanisms, *J. Atmos. Terr. Phys.*, *58*, 1769.

Schoendorf, J., G. Crowley, R. G. Roble, and F. A. Marcos (1996b), Neutral density cells in the high latitude thermosphere—1. Solar maximum morphology and data analysis, *J. Atmos. Terr. Phys.*, *58*, 1751.

Schunk, R. W., and A. F. Nagy (2000), *Ionospheres*, Cambridge Univ. Press, New York.

Schunk, R. W., and J. J. Sojka (1996), Ionosphere-thermosphere space weather issues, *J. Atmos. Terr. Phys.*, *58*, 1527.

Sojka, J. J., and R. W. Schunk (1983), A theoretical study of the high latitude F regions response to magnetospheric storm inputs, *J. Geophys. Res.*, *88*, 2112.

Sojka, J. J., R. W. Schunk, and W. J. Raitt (1981), Plasma density features associated with strong convection in the winter high-latitude F region, *J. Geophys. Res.*, *86*, 6908.

Sojka, J. J., M. David, and R. W. Schunk (2002), A mid-latitude space weather hazard driven directly by the magnetosphere, *J. Atmos. Sol. Terr. Phys.*, *64*, 687.

Tsagouri, I., G. Moraitis, and H. Mavromichalaki (2000), Positive and negative ionospheric disturbances at middle latitudes during geomagnetic storms, *Geophys. Res. Lett.*, *27*, 3579.

Weimer, D. R. (1996), A flexible, IMF dependent model of high-latitude electric potential having "space weather" applications, *Geophys. Res. Lett.*, *23*, 2549.

Yin, P., C. N. Mitchell, P. S. J. Spencer, and J. C. Foster (2004), Ionospheric electron concentration imaging using GPS over the USA during the storm of July 2000, *Geophys. Res. Lett.*, *31*, L12806, doi:10.1029/2004GL019899.

—————————

Y. Deng and A. J. Ridley, Center for Space Environment Research, University of Michigan, Ann Arbor, MI 48109-2143, USA. (ydeng@umich.edu; ridley@umich.edu)